

Long-lived ionic nano-domains can modulate the stiffness of soft interfaces

Supplementary information

William Trewby¹, Jordi Faraudo², Kislun Voitchovsky¹

Contents

| | | |
|-------|--|----|
| 1 | Sample preparation..... | 2 |
| 1.1 | Cleaning of apparatus and glassware..... | 2 |
| 1.2 | Small unilamellar vesicle (SUV) suspensions | 2 |
| 1.3 | Supported lipid bilayers..... | 2 |
| 2 | Electrophoretic measurements | 4 |
| 2.1 | Supporting theory and experimental procedure | 4 |
| 2.2 | Calculation of binding constants for cations..... | 5 |
| 3 | Atomic force microscopy (AFM)..... | 8 |
| 3.1 | Cantilever and sample preparation | 8 |
| 3.2 | Small-amplitude AFM imaging | 8 |
| 3.2.1 | Impact of cantilever | 11 |
| 3.2.2 | Variation of stiffness and cation adsorption with pH..... | 12 |
| 3.3 | Phase difference spectroscopy | 13 |
| 3.4 | Bimodal AFM imaging..... | 14 |
| 3.5 | Static force spectroscopy | 16 |
| 4 | Image analysis..... | 18 |
| 4.1 | Roughness..... | 18 |
| 4.2 | Nearest neighbours distribution | 19 |
| 4.3 | Ionic decorrelation time, τ | 20 |
| 5 | Molecular dynamics (MD) simulations | 21 |
| 5.1 | Methods, description of simulated systems and simulation protocol..... | 21 |
| 5.2 | Analysis of MD results: technical details and additional results..... | 22 |
| 6 | Supplementary References..... | 27 |

¹ University of Durham, DH13LE, UK. Correspondence: kislun.voitchovsky@durham.ac.uk

² Institut de Ciència de Materials de Barcelona, Spain

1 Sample preparation

1.1 Cleaning of apparatus and glassware

A day prior to the each experiment, the 5 ml glass vials, glass petri dish, tweezers, mini-extruder kit and 1 ml syringes (Avanti Polar Lipids, AL, USA) were bath sonicated for > 10 minutes in ultrapure water (Merck-Millipore, 18.2 M Ω resistivity). The fluid was exchanged for isopropanol (Fisher Chemical, certified ACS, \geq 99.5% purity) and the apparatus was sonicated for a further 10 minutes to remove any contaminant organic material. The isopropanol was drained, the equipment was rinsed thoroughly with ultrapure water until no observable trace of the solvent remained and it was then sonicated in the ultrapure water for 10 minutes. Finally, the water was drained and the equipment was covered and allowed to dry completely at a temperature of 40°C

1.2 Small unilamellar vesicle (SUV) suspensions

1,2-dipalmitoyl-sn-glycero-3-phosphate (DPPA) (Avanti Polar Lipids, AL, USA) was purchased in powder form and used without further purification. A mass of \sim 1 mg of DPPA was measured into a 5 ml glass vial and diluted to a lipid concentration of 1 mgml⁻¹ with 150 mM NaCl (ACS reagent grade, \geq 99%, Sigma Aldrich). For the electrophoretic measurements, the salt concentration and type was to be varied, so we carried out the below procedure with the lipids suspended in ultrapure water buffered with 5 mM sodium phosphate dibasic (\geq 99.0%, Sigma Aldrich) to a pH of 7.45. The buffer was necessary because evaluation of the binding constants of each ion (see below) requires precise knowledge of the concentration of protons in solution. Buffering agents were not used as part of the AFM experiments because these have been shown to alter the hydration structure at hydrophilic interfaces and interfere with high-resolution AFM imaging¹. The solution was bath-sonicated for 30 minutes at 55°C, resulting in it taking on a milky, opaque colour due to the formation of multilamellar vesicles. The vesicles were held at -18°C for 30 minutes, and then sonicated at 55°C for the same period of time, resulting in a uniform, transparent solution. This “freeze-thaw” method encourages the break-up of larger vesicles and tends to result in more well-defined, smaller lipid assemblies². In the case of producing supported bilayers (section 1.3), the solution was then diluted further with 150 mM NaCl to a final lipid concentration of 0.1 mgml⁻¹. The cleaned extruder (section 1.1), along with a polycarbonate 100 nm membrane (WhatMan, Sigma Aldrich) were used to extrude the lipid vesicles at least 15 (but always an odd number) times at 70°C (in our case, the melting temperature for DPPA was $T_m \sim 67^{\circ}\text{C}$ ³). This results in a monodisperse SUV suspension, with vesicles of \sim 100 nm diameter. For the electrophoretic measurements (section 2), the lipid solution was extruded at the higher concentration of 1 mgml⁻¹, and then diluted to 0.1 mgml⁻¹ with the appropriate mix of ultrapure water and 150 mM monovalent salt to give the required ionic strength. The solution was then either used directly, or sealed in a glass vial and refrigerated for a maximum of one week.

1.3 Supported lipid bilayers

Having produced the SUV suspension, the vesicle fusion method⁴⁻⁶ was then utilised to produce supported lipid bilayers for the AFM experiments. This process involves pipetting the vesicle solution onto a stiff, hydrophilic support – in our case, muscovite mica (grade IV, SPI Supplies, PA, USA). The ensemble is then

heated above the lipids' melting point (such that they are in the liquid disordered, L_α , phase). The inclusion of salts acts to screen electrostatic interactions between the vesicles and the substrate⁵, allowing the two to come into close contact. Once this occurs, the elevated temperature and the small radius of curvature of the vesicles encourages the lipids to spread spontaneously across the substrate, forming planar lipid bilayers on the mica.

The muscovite mica support had previously been affixed to a steel support with epoxy glue and cured at 60°C for at least four hours. The mica was cleaved 3 times with adhesive tape or until mirror-smooth to the naked eye. After extrusion, approximately 80 μl of the DPPA vesicle solution (see above) was pipetted onto the mica and the entire sample was incubated in a sealed glass petri dish with a damp cotton pad (to reduce evaporation of the sample) at 80°C. The sample was then cooled at a rate of 2°C h⁻¹ to 60°C, and then cooled to 25°C at around 6°C h⁻¹. The purpose of this elongated heating ramp was to ensure the lipids went through their phase transition from liquid disordered (L_α) to solid ordered (L_β) state as close to equilibrium as possible, greatly reducing the possibility of a kinetically trapped, glassy state similar to that of the “ripple phase”⁷. This procedure reliably produced at least one defect-free DPPA bilayer on the mica surface that could be checked via AFM, by applying large normal forces while scanning in contact mode to create holes in the membrane (see Fig. S 1).

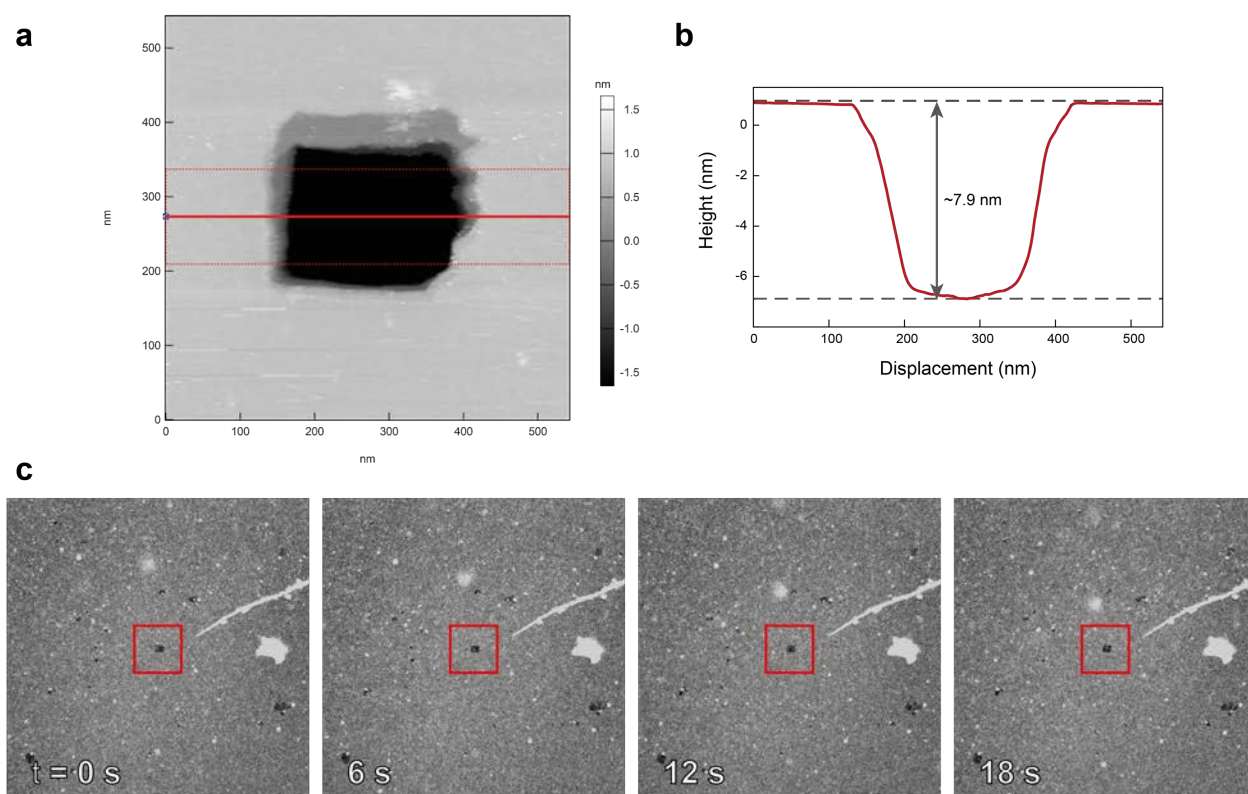


Fig. S 1 | Verifying the formation of DPPA supported lipid bilayers. (a) (550 × 550) nm² topographic image showing the result of scanning a smaller area under “harsh” conditions in contact mode. The tip has clearly created a defect in the bilayer that extends down to the mica below. A section is taken at the thick red line that is laterally averaged between the two dashed red lines (b). The depth of the defect is double that expected for a bilayer, showing that our procedure has produced a stack of two membranes on the mica. (c) Representative (500×500) μm^2 confocal microscopy scans of a fluorescently-labelled DPPA membrane with a central region of (10×10) μm^2 bleached by repeated scanning (red boxes). The bleaching as well as the lack of recovery over 3 minutes confirms that the background fluorescence comes from a well-formed DPPA bilayer. Bright defects in centre-right of images were manually created with a sharp needle to create a reference point.

The robustness of this procedure to produce supported lipid bilayers on macroscopic lengthscales was further verified by fluorescence microscopy. This required including a fluorescently labelled lipid probe – 1,2-dipalmitoyl-*sn*-glycero-3-phosphoethanolamine-N-(lissamine rhodamine B sulfonyl), (16:0 Liss Rhod PE, Avanti Polar Lipids, AL, USA) – in the bilayer at a concentration of 0.1 mol%, a sufficiently low concentration such that the bilayer behaviour would not be significantly perturbed. The fluorescent probe was purchased in chloroform solution, which was thoroughly evaporated before combining with the correct mass of DPPA in power form. An identical procedure to that of the main script was then followed to produce supported lipid bilayers on mica before loading into an EZ-C1 Confocal Microscope (Nikon UK, Kingston, UK) and imaging in reflection mode. A small, (10×10) μm^2 region was raster-scanned repeatedly in order to bleach the rhodamine molecules, before imaging a zoomed-out region of (500×500) μm^2 at a rate of 1 s/image and a delay of 2 s between images (see Fig. S 1c, selected images shown). The presence of a bleached square (red boxes) that did not recover over the full 180 s of scanning (full data not shown) confirmed the successful formation of a large-scale gel-phase DPPA membrane on the mica surface.

2 Electrophoretic measurements

2.1 Supporting theory and experimental procedure

The electrophoretic mobility, μ , of the DPPA vesicles was measured using a Zetasizer Nano ZS (Malvern Instruments, Worcestershire, UK) with a 4 mW He-Ne laser. In brief, the technique applies an oscillating potential difference, V , of the order of a few tens of Volts to the SUVs *via* two gold electrodes at the top of the cell. The negatively-charged liposomes then drift in response to the external electric field, with a velocity, v , proportional to the potential at their slip plane – i.e. their zeta-potential, ζ ⁸;

$$\mu \equiv \frac{v}{V} = \frac{2\varepsilon_0\varepsilon_r f(\kappa a)}{3\eta} \zeta. \quad (1)$$

Here, η is the solution's viscosity, ε_0 is the permittivity of free-space and ε_r is the relative permittivity of the solution. The Henry function, $f(\kappa a)$, is a continuous function of the Debye length, κ^{-1} ⁹,

$$\kappa^{-1} = \left(\sum_i \frac{\varepsilon_0\varepsilon_r k_B T}{\rho_{i,\infty} e^2 z_i^2} \right)^{\frac{1}{2}}, \quad (2)$$

and the vesicle radius, a . The bulk density of ionic species i with valency z_i is given by $\rho_{i,\infty}$ and k_B , T and e are the Boltzmann constant, absolute temperature and charge on the electron respectively. The Debye length governs the size of the diffuse layer of ions close to the lipid bilayer and if this is much smaller than the vesicle radius (Smoluchowski limit, $\kappa a \gg 1$), the Henry function $f(\kappa a) = 1.5$. If the Debye length is large relative to a (Hückel limit, $\kappa a \ll 1$), $f(\kappa a) = 1.0$. As the Debye length strongly depends on the solution's ionic strength, I ,

which was varied as part of the experiment, neither of these limits was valid across the entire range of concentrations tested ($0 \leq I \leq 145$ mM), and so a smooth function was assumed in a similar fashion to Maity *et al.*¹⁰:

$$f(\kappa a) = \begin{cases} 1, & \kappa a < 1 \\ 1/6 \log(\kappa a) + 1, & 1 < \kappa a < 1000 \\ 1.5, & \kappa a > 1000 \end{cases} \quad (3)$$

The relative permittivity, ϵ_r , and viscosity, η , were estimated for each concentration using the “solvent builder” incorporated into the Zetasizer ZS software.

Measurement cells were initially rinsed with ultrapure water, followed by isopropanol and finally with ultrapure water once more, prior to the vesicles coming into contact with them. Approximately 100 μl of the 0.1 mgml^{-1} vesicle solution was pipetted into a disposable low volume cuvette for the purposes of measuring a , and another 1 ml was transferred into a folded capillary zeta cell (both Malvern Instruments, Worcestershire, UK) to find ζ .

The vesicles’ radii was determined through dynamic light scattering (DLS). This technique records backscattered light (to an angle of 173°) from the solution and measures its autocorrelation function. Because the fluctuation of the scattered light is due to the Brownian motion of the vesicles in solution, the timescale of an exponential function fit to the autocorrelation can be related to the diffusion coefficient, D , of the particles. The Stokes-Einstein relation,

$$a = \frac{k_B T}{3\pi\eta D}, \quad (4)$$

then allows the particle radius to be calculated.

The vesicles’ mobility is determined by laser-doppler interferometry. Here, two coherent laser beams are made to intersect in the sample cell at one of the stationary planes (where the net velocity is zero). The interference fringes generated are made to flicker due to vesicles passing across the interference plane, and the flicker frequency is used to infer their velocity. The ζ -potential value in each ionic solution is the average of three measurements and errors were calculated from their standard deviation.

2.2 Calculation of binding constants for cations

The link between the measured ζ -potential and bilayer surface charge density was achieved by combining the well-known Boltzmann distribution of ions in solution, $\rho_x = \rho_\infty \exp(-e\psi_x/k_B T)$ with the Poisson equation, $e\rho_x = -\epsilon_0\epsilon_r(d^2\psi_x/dx^2)$ to arrive at the Grahame equation⁹,

$$\sigma = \sqrt{8\epsilon_0\epsilon_r\rho_\infty k_B T} \sinh\left(\frac{e\psi_0}{2k_B T}\right), \quad (5)$$

which is valid for monovalent symmetric salts of bulk density ρ_∞ . Here, the surface charge density is given by σ , the electric potential at the vesicle-electrolyte interface is given by ψ_0 , and ψ_x, ρ_x are the potential and ionic density at perpendicular height x above the lipids respectively. Equation 5 allows the surface charge density to be found solely from the bulk concentration of ions and the surface potential.

It is well accepted that the zeta-potential refers to the potential at the ill-defined hydrodynamic “slip plane” that depends on the nature of the interface as well as κa ⁸. However, it has been shown that assuming the plane of shear to be 2 Å from the lipid headgroups gives consistent values of ζ -potential/binding constant for metal cations^{11,12} and agrees well with our assumptions about the nature of the Stern layer in the subsequent AM-AFM experiments. Therefore, we can use the expression for the x dependence of the potential derived again from the Poisson and Boltzmann expressions⁹,

$$\psi(x) = \frac{2k_B T}{e} \log \left[\frac{1 + \gamma \exp(-\kappa x)}{1 - \gamma \exp(-\kappa x)} \right], \quad (6)$$

where $\gamma \equiv \tanh(e\psi_0/4k_B T)$, to relate the zeta potential (i.e. ψ at $z = 2$ Å) to the surface potential, ψ_0 .

Once the total charge density, σ_{tot} , is known, the charge due solely to adsorbed ions, σ_{ion} is simply found from $\sigma_{\text{ion}} = \sigma_{\text{H}_2\text{O}} - \sigma_{\text{tot}}$, i.e. the difference between the charge density in pure water and in the ionic solution. Finally, the fractional ionic coverage is found by calculating the number of adsorbed ions per lipid, Γ , via

$$\Gamma = \frac{\sigma_{\text{ion}}}{e\rho_1}, \quad (7)$$

where $\rho_1 \sim 4 \times 10^{18} \text{ m}^{-2}$ is the surface density of the lipid molecules, as calculated from the AFM topographs shown in Fig. 1 of the main text and Fig. S 3. We observe that ρ_1 does not vary with the type of ion in solution (see Fig. 1 and

Table II). Γ is plotted versus bulk concentration for NaCl, KCl and RbCl in Fig. S2Fig. S 1. Binding constants were calculated assuming a Frumkin-Fowler-Guggenheim adsorption model¹³. This relates Γ for each ion to their binding constant with the membrane, K , the affinity of protons for the lipids’ phosphate headgroup, $pK_a = 8.0^3$, and their bulk density, C in moles:

$$\Gamma = \frac{KC \exp(nE_c \Gamma / k_B T)}{1 + KC \exp(nE_c \Gamma / k_B T) + pK_a [\text{H}^+]}. \quad (8)$$

Here, the bulk ionic strength, C , and proton/hydronium concentration, $[\text{H}^+]$, are in moles, and n is the number of nearest neighbours of each binding site; we assume here that the lipids are hexagonally close-packed and that adsorbed ions form a 2D monolayer – i.e. $n = 6$. This is, however, an over-simplified picture of the interface. E_c represents the effective correlation energy between ions at the interface and so accounts for hydration- and lipid-mediated interactions that affect ions’ adsorption to the membrane. If $E_c < 0$, the ions experience attractive interactions between themselves; if $E_c > 0$, there is a mutual repulsion and if $E_c = 0$, then equation 8 reduces to the Langmuir adsorption model of a 2D gas. Equation 8 was fitted to the data in Fig. S2, with E_c and K used as fitting parameters. Errors were taken from the fitting uncertainties in Wavemetrics’ Igor programme (v6.3.7.2).

The fits to equation 8 for each ion are shown in Fig. S2(a) as dashed lines and describe the data very well, highlighting the suitability of the FFG model for describing the vesicle-cation interaction. The respective values of K extracted from the fits are displayed in Fig. S2(b) and Table I and indeed show that the ions' binding strength is dictated by their atomic weight – i.e. they display Hofmeister-like ordering; $K_{\text{Na}^+} > K_{\text{K}^+} > K_{\text{Rb}^+}$. The relative strengths and order of magnitude agree very well with previous measurements of binding constants to anionic lipids^{12,14}. Reported absolute values tend to be a little lower ($K \leq 1.0$) but we note that our model system is in gel phase and thus has a smaller area per lipid (greater charge density), which is likely to encourage ion binding. The correlation energies are also shown in Table I and are all negative, demonstrating that the ions experience an attractive interaction amongst the lipid headgroups, despite their similar charges.

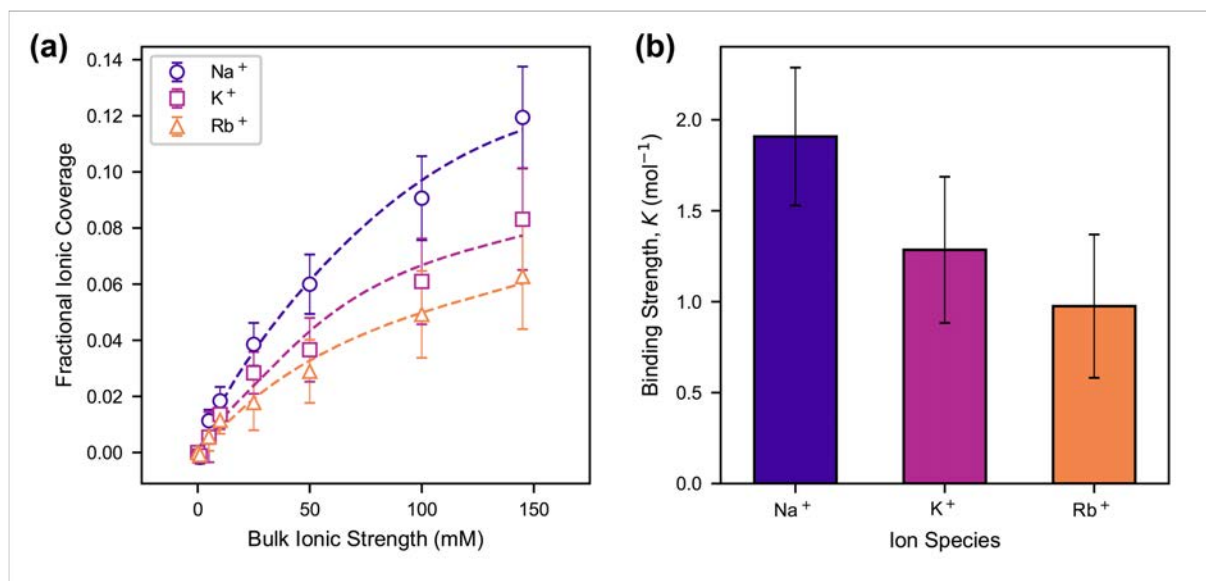


Fig. S 2 | (a) Ionic coverage profiles of ~100 nm diameter DPPA vesicles in varying salt solutions, calculated from their electrophoretic mobility as described in the text. In all cases, increasing the total salt concentration results in an increase in adsorbed charge but the extent to which this happens depends strongly on the type of cation in the solution. Dashed lines represent a fit to the data with equation 8. Binding constant, K , extracted from the fitting is shown for each ion in (b)

The value of increases with ion size (albeit with large uncertainty) which emphasises the role of hydration interactions; sodium has the highest charge density and so the electrostatic energy is larger relative to water-driven attraction. Conversely, rubidium's large size results in a reduced electrostatic contribution, allowing correlative interactions to play a greater part, and increasing E_c .

| Cation | Binding constant, K (mol ⁻¹) | Correlation energy, E_c ($k_B T$) |
|-----------------|--|---------------------------------------|
| Na ⁺ | 1.9 ± 0.4 | -1.1 ± 0.4 |
| K ⁺ | 1.3 ± 0.4 | -1.6 ± 0.9 |
| Rb ⁺ | 1.0 ± 0.4 | -2 ± 2 |

Table I | Binding constants and energies of correlation extracted from FFG isotherms of Fig. S2(a) (dashed lines). The binding constants decrease with ionic radius as has been observed previously in lipid systems. Intriguingly, all E_c values are negative, indicating an attractive potential between the adsorbed ions, and this value *increases* with the atomic size of the alkali metal.

3 Atomic force microscopy (AFM)

The AFM images and spectroscopy curves were all collected using a commercial Cypher ES AFM (Asylum Research, Santa Barbara, USA) using Arrow UHF AuD cantilevers (Nanoworld, Neuchâtel, Switzerland), which have tips with nominal radii of curvature of less than 10 nm. The stiffness of the cantilever used to produce the images and data of Fig. 1 and 3 was $k_1 = 1.71 \text{ Nm}^{-1}$, calibrated from its thermal spectrum¹⁵. The cantilevers used to produce the bimodal images and static Young's modulus values had stiffnesses of $k_1 = 0.956 \text{ Nm}^{-1}$ and $k_1 = 6.58 \text{ Nm}^{-1}$ respectively.

3.1 Cantilever and sample preparation

A day prior to imaging, the cantilever was rinsed in isopropanol. Next, the cantilever and cantilever holder were bathed in isopropanol overnight (> 12 hours), followed by rinsing and bathing in ultrapure water for at least 30 minutes. This serves to remove any organic material or silicon oil from the tip that may have accumulated during its storage in its gel box^{16,17}, while minimising any alteration of tip geometry/size. The cantilever and tip were then wetted with $\sim 50 \mu\text{l}$ of 150 mM NaCl.

The supported lipid bilayers (see section 1.3) were removed from the oven at room temperature and rinsed by repeatedly pipetting $50 \mu\text{l}$ of 150 mM NaCl into the fluid on top of the mica disc and then taking out the same volume. This procedure removes any unfused vesicles and ensures that the imaging solution is as clean as possible. The cantilever and sample were then brought into close proximity, such that a capillary bridge was formed between the two fluids, and the images and force spectroscopy curves were subsequently collected.

When sufficient data had been acquired in the NaCl solution, the tip and sample were separated, with care taken to keep the SLB immersed at all times. The NaCl was then replaced with 150 mM KCl by rinsing $50 \mu\text{l}$ at a time, with at least $500 \mu\text{l}$ total fluid exchanged (~ 8 times the volume initially on the disc). Images and force curves were collected as before, and the procedure was then repeated for 150 mM RbCl.

3.2 Small-amplitude AFM imaging

As discussed in the main text, the images were collected in amplitude-modulation mode while fully immersed in each salt solution. This was achieved by photothermally driving the cantilever close to its fundamental resonance frequency. The cantilever's oscillation amplitude, A , is sensitively linked to the interaction between the tip and sample¹⁸ and by keeping this constant with a feedback loop, the topography of the sample can be recorded with sub-Ångström precision. The phase difference between the driving sinusoidal signal and the cantilever oscillation was allowed to vary freely and gives information about the energy dissipated by the tip as it moves through its cycle¹⁸. As only the phase *difference* is a measurable quantity, its absolute value was set to 90° when far from the sample.

The imaging was conducted with free (that is, when not interacting with the sample) amplitudes, A_0 , of 1-2 nm. The ratio between the working amplitude, A_w , used as part of the feedback loop and the free amplitude is

known as the setpoint ratio, S_p , and was maintained at $S_p \equiv A_w/A_0 \geq 70\%$ in order to mainly probe the fluid at the bilayer-electrolyte interface (see main text and references therein). Multiple images were taken in each ionic solution to confirm the effects observed in Fig. 1 in the main text were consistent and reproducible.

Representative topography (purple/yellow) and phase (blue/black) images are displayed in Fig. S 3, which show similar features to those observed in the main text. When imaged in NaCl, the regular hexagonal symmetry of the lipids is superposed with mesh-like regions of higher topography that can distort or otherwise alter the symmetry observed. These meshes contribute to the higher roughness, R_q , of images in sodium as compared to potassium and rubidium. The phase signal is also heterogenous, displaying corrugations that somewhat align with variations in height. However, in general the individual lipid sites are more clearly resolved in the phase. This is a reflection of the nature of AM-AFM imaging – despite the ions’ formation of an amorphous mesh on top of the lipids which distorts the height trace, the energy dissipated by the tip per oscillation varies strongly between sites, leading to greater phase contrast. The images taken in potassium chloride demonstrate a comparable heterogeneity in height, but with a much-reduced R_q . The apparent symmetries (i.e. rows or individual sites) are in general much more consistent than those acquired in sodium, although there are some occasions (upper section of third and fourth images) where there is an abrupt change. This was assumed to be due to the probe effectively imaging different hydration shells, which can result in changes in symmetry¹⁹. The third row illustrates images that were taken in RbCl solution. Further single-ion adsorption events can be observed in these images, visible as bright white blobs often overlapping two molecular rows. The adsorption of large rubidium cations results in much larger variations in the height, reflected in the colour scale of 125 pm for these images and the extent to which these ions perturb the hydration landscape also resulted in much greater variations in the phase. However, the roughness, R_q of the images was in fact slightly lower than that in NaCl (0.032 ± 0.004 nm compared to 0.037 ± 0.003 nm), demonstrating the dominant impact of the cohesive Na^+ layer on interfacial topography.

The insets of Fig. S 3 show the fast Fourier transform power spectrum corresponding to each phase trace. The lattice parameters were measured from these to be ~ 4.5 Å and did not vary significantly from image to image, or in different solutions, in agreement with the MD simulations (see section 5 and

Table III). While these dimensions are somewhat smaller than those measured for free-standing DPPA bilayers²⁰, this is likely due to specific interactions with the solid substrate, and our results coincide with other molecular-level AFM measurements of bilayers formed on mica^{21,22}.

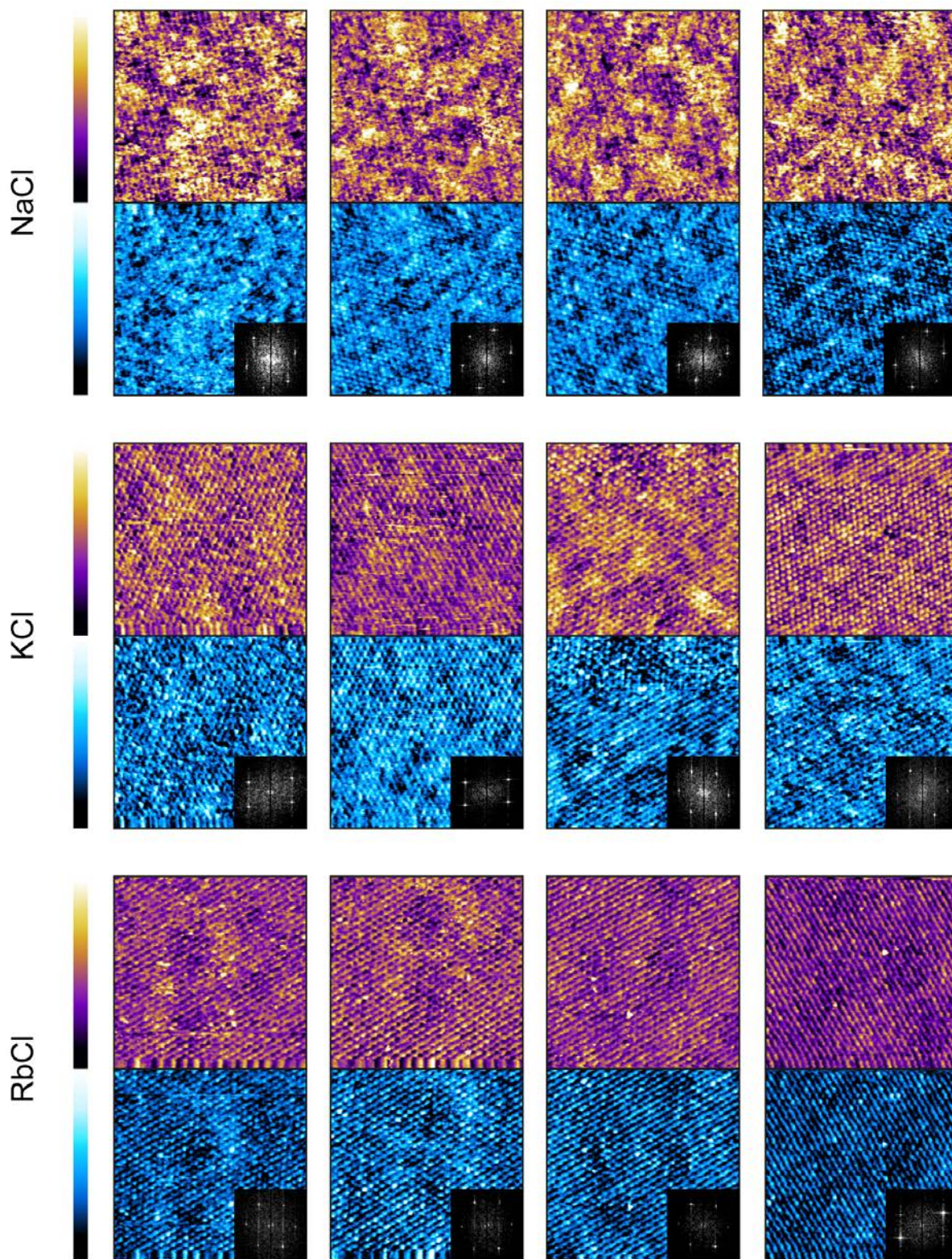


Fig. S 3 | Additional (15×15) nm² high-resolution AM-AFM images in each solution used, illustrating the consistent effects of each ion on the apparent topography (purple/yellow) and phase (blue/black). For NaCl and KCl the topography and phase scale bars cover 110 pm and 5° respectively. For RbCl, they cover 125 pm and 11°. The power spectrum of each phase image are shown in its lower-right corner.

3.2.1 Impact of cantilever

AM-AFM imaging is necessarily a perturbative technique, with the nano-sharp tip probing the interface once every few microseconds. Hence we accept that the ionic structures observed at the lipid headgroups will not be equilibrium structures and some adsorbed ions will be removed as part of the imaging process. We aimed to mitigate tip-specific effects as much as possible by using the same cantilever throughout the experiment and imaging with a “soft” setpoint ratio of $S_p \geq 70\%$. This ensured that comparisons between the images in each electrolyte were meaningful and represented genuine differences between ion-lipid interactions. However, the question of the *extent* to which the cantilever disturbs the strongly-ordered Stern layer still remains. To tackle this, we prepared supported lipid bilayers in an identical manner to those used to produce Fig. 1, 3 and S3. We then imaged the lipid bilayer in a 150 mM RbCl solution using a cantilever (OMCL-RC800PSA; Olympus, Japan) with a spring constant of $k_1 = 0.7 \text{ N m}^{-1}$, less than half that of that of the original cantilever used. The small-amplitude imaging parameters were also kept identical so that, to as great an extent as possible, changes observed in topography were solely due to the difference in spring constants. A comparison between images produced with each cantilever is shown in Fig. S 4.

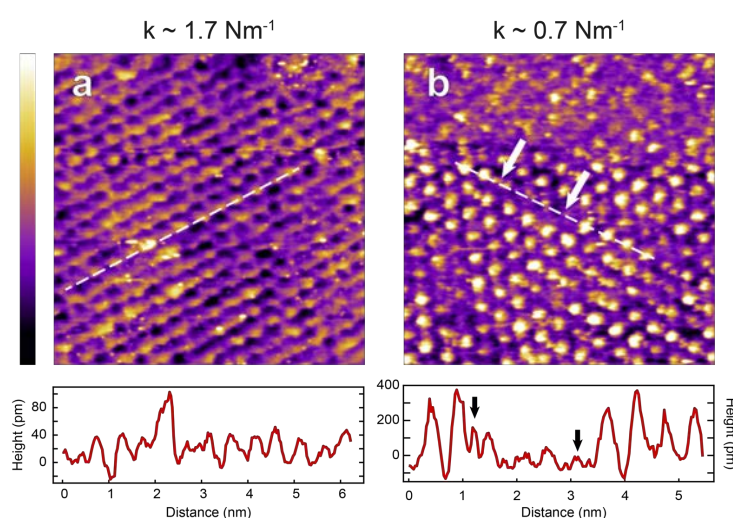


Fig. S 4 | Comparison between imaging using a high ((a), $k_1 \sim 1.71 \text{ N m}^{-1}$) and low ((b), $k_1 \sim 0.7 \text{ N m}^{-1}$) stiffness cantilever. (7.5×7.5) nm^2 topography traces of a DPPA bilayer immersed in 150 mM RbCl. The colour scale in (a) and (b) represent 120 pm and 350 pm respectively. The sections (white dashed lines) are presented below each image and the white arrows’ location on the image correspond to the black arrows in the section.

Both images display the topography of the rubidium/lipid interface and thus have similar lattice symmetries and parameters. However, as can be seen from the section taken along each image (white dashed line) the scales differ greatly, with (a) having a total range of approximately 120 pm and (b) spanning 350 pm. The symmetries presented are also distinct; (a) displays mostly row-like corrugations with low height differences, while (b) clearly shows individual circular protrusions that have at least twice the height of those in the former. This reinforces the conclusions made in the main text; using a stiffer cantilever dissipates more energy into the interface, thus removing the majority of weakly-adsorbed rubidium ions. Hence the topography is in fact dominated by oriented water and hydronium with occasional Rb^+ ions surviving interrogation by the AFM tip. Using a softer cantilever mitigates this effect and we instead observe mostly well-adsorbed Rb^+ ions (as evidenced by their large size relative to the lipid bilayer) with many fewer “defects” in their arrangement. These desorption events are highlighted in Fig. S4 with arrows on the image and section.

3.2.2 Variation of stiffness and cation adsorption with pH

As discussed in the main text, the variation of lipid membrane stiffness with ion type, and the corresponding variation of binding mode (Fig. 4c and 2d, respectively) imply that increasing the concentration of an ion that binds in a predominantly inner-sphere configuration will stiffen the bilayer. To quantify this, we performed static force spectroscopy and small-amplitude AFM imaging on a supported DPPA membrane at varying pH. The conditions were otherwise identical to those of Fig. 1a (Arrow UHF cantilever, 150 mM NaCl solution). As discussed in section 1.2, the use of buffering agents introduces ionic species into solution that interfere with the interfacial landscape and would influence the apparent topography¹ and so we titrated the ultrapure water with HCl/NaOH alone. The pH of each solution was measured immediately before and after the experiment to ensure that it did not change significantly due to atmospheric CO₂. The solutions were changed sequentially, by withdrawing the cantilever and rinsing the sample thoroughly ($5 \times 50 \mu\text{l}$) with the new imaging buffer. The static force spectroscopy results are shown in Fig. 4c of the main text. Increasing the pH – that is, decreasing the concentration of hydronium ions in solution – strongly reduces the effective stiffness of supported DPPA membranes. The representative images collected in the same experiment are shown in Fig. S 5. They support our conclusion; namely that at high concentrations, H₃O⁺ ions compete with Na⁺ for access to the PA⁻ headgroups of the lipids. Thus, the topography appears much rougher and the imaging is less stable for low pH. As the pH is increased to 5.6, the imaging is more stable (with fewer horizontal artefacts) but the topography is still rough and covers a large height range. Imaging in pH 6.6 and 7.0, conversely produces a remarkably regular interface that has much less variation, due to the Na⁺ being allowed to form a more complete coverage on the lipid bilayer.

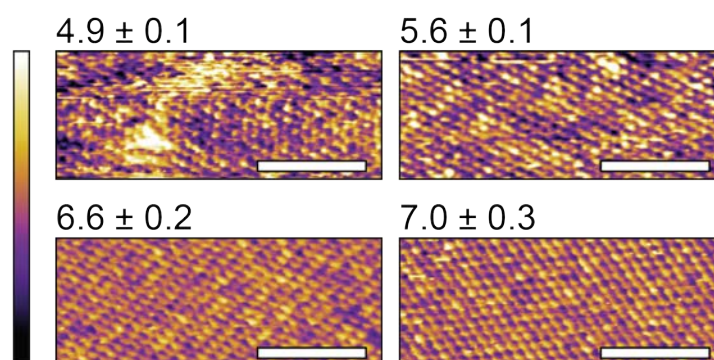


Fig. S 5 | AFM topography images of the DPPA bilayer in 150 mM NaCl solution (collected during the same experiment as that of Fig. 4d) at different pH values that are noted above each image. At low pH, there is a high concentration of protons or H₃O⁺ ions that compete for inner-sphere binding sites with Na⁺. The smaller size and faster diffusion of the hydronium renders the interface more rough and the imaging less stable than if there were sodium alone. As the pH is increased, the sodium can adsorb more readily, leading to the regular, flatter topography observed in pH of 6.6 and 7.0. In each image, the length scale bar represents 5 nm and the colour scale covers 150 pm

3.3 Phase difference spectroscopy

The “phase residuals” presented in Fig. 1d were acquired by performing force spectroscopy in amplitude-modulation mode on the lipid bilayers in each electrolyte solution. The cantilever was driven to oscillate at smaller amplitudes compared to those used for imaging (~ 250 pm), and its deflection, amplitude and phase difference were tracked as a function of z -piezo extension. At least 15 such phase-spectroscopy curves were taken in each electrolyte solution and aligned using an automated routine. As such, the deflection trace’s inflection point was found by the least-squares-minimisation of two simultaneous straight-line fits, and this was inferred to be the contact point (i.e. $z = 0$). The long-range ($z < -1.5$ nm,) interactions were also subtracted from the deflection trace. Once this had been carried out, the true tip-lipid separation, d_{tl} was computed using the standard relation for AFM spectroscopy: $d_{tl} = z - \Delta D$, where z is the extension of the z -piezo (i.e. cantilever) and ΔD is the change in deflection, after alignment. As mentioned earlier, the cantilever’s motion far from the lipid bilayer ($z < -1.5$ nm) was assumed to be totally viscous, and so the phase was offset to be 90° in this region.

An illustration of this procedure given in Fig. S 6, for a DPPA bilayer in 150 mM KCl. As the cantilever approaches the lipids, the increased tip-sample interaction acts to smoothly reduce the oscillation phase, indicating that more energy is being dissipated into the interfacial layers of fluid, before the tip comes into contact with the bilayer (indicated by the sharp increase in deflection). As well as a smooth decrease, the phase demonstrated reproducible “steps” that deviated from the approximately sigmoidal function. These occurred before full-contact with the bilayer and indicate an anomalous dissipation of energy by the AFM tip that we associate with the removal of an adsorbed cation from the lipid headgroups. This is in accordance with Ricci *et al.*’s results²³ on calcite, where discontinuities in phase and amplitude could be induced by the presence of 10 mM NaCl in the imaging fluid. We note that the steps in our data are much more reproducible, most likely due to the higher concentration of ions in our solution. A total of at least 15 curves were collected on the supported lipid bilayer in each solution. The phase, $\theta(z)$, curves were each fitted with a sigmoidal function of the form

$$\theta(z) = \theta_0 + \frac{\theta_{\max}}{1 + \exp((z_{\text{half}} - z)/\lambda)}, \quad (9)$$

where θ_0 and θ_{\max} are the baseline and maximum phases respectively and z , z_{half} and λ are the z -piezo’s height, height-at-half-phase and decay rate of the sigmoid respectively. The function was then subtracted from the averaged, aligned spectroscopy curves and they were then plotted against the tip-lipid separation, d_{tl} , to produce the residuals of Fig. 1d.

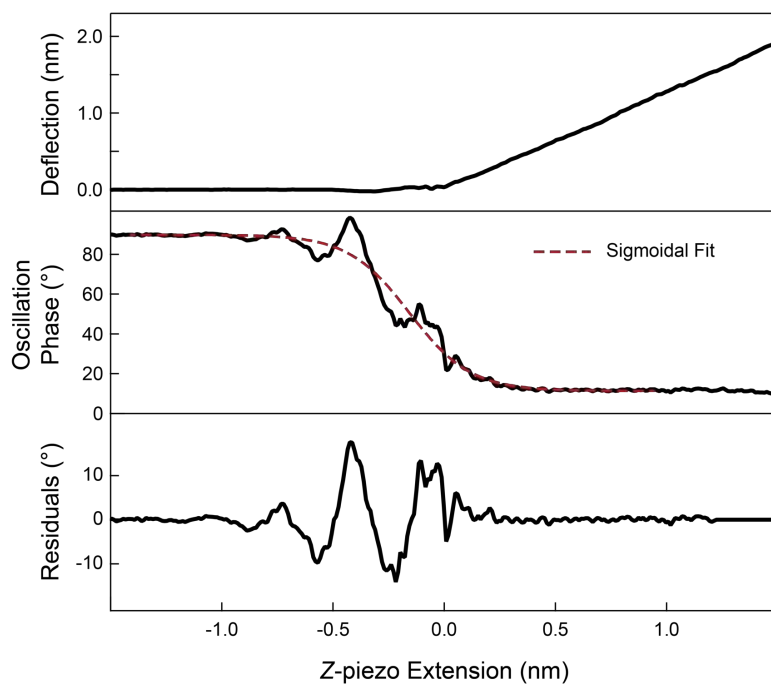


Fig. S 6 | AM-AFM spectroscopy signals recorded on the DPPA bilayer in 150 mM KCl solution. Deflection (upper), oscillation phase difference (middle) and the sigmoidal fit residuals (bottom) are plotted versus the extension of the z -piezo, such that $z \ll 0$ represents bulk electrolyte. As the AFM tip comes into hard contact with the bilayer the increased tip-sample interaction damps the phase. The strongly adsorbed ions induce characteristic peaks in the phase that are highlighted by the subtraction of a sigmoidal fit. The traces represent the averages of at least 15 force spectroscopy curves that have been aligned *via* an automated algorithm. The average deflection and phase far from the sample ($z < -1.5$ nm) were offset to 0 nm and 90° respectively.

3.4 Bimodal AFM imaging

As discussed in the main script, bimodal AFM involves the excitation of the fundamental and second resonance mode of the cantilever simultaneously (ν_1 and ν_2 in Fig. S 7) in order to extract the effective Young's modulus, E_{eff} , of the interface. The fundamental mode is controlled exactly as earlier – that is, in amplitude modulation mode – while the second mode is controlled via frequency modulation (FM). This requires keeping the second mode's phase, θ_2 , locked to 90° by adjusting ν_2 . As long as the second mode's amplitude is small relative to that of the fundamental, this technique can be used to extract E_{eff} with errors $< 5\%$ while maintaining molecular-level lateral resolution by following the procedure of Amo *et al.*²⁴.

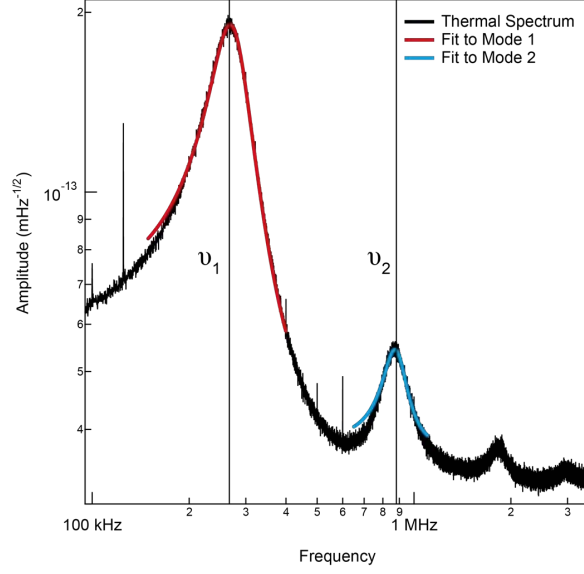


Fig. S 7 | Thermal spectrum of Arrow UHF AuD cantilever used to collect bimodal images presented in Fig. 4 of the main text. The first and second resonance frequencies have been highlighted and simple harmonic oscillator fits to these are shown in red and blue respectively. These fits were used to derive the cantilever properties $k_1 = 0.956 \text{ Nm}^{-1}$, $Q_1 = 3.3$ and $k_2 \sim 7.07 \text{ Nm}^{-1}$. Here, there is no well-characterised method for calculating k_2 , especially for such unconventional cantilever shapes²⁵ and so the value was estimated from a thermal fit to the second mode with the same inverse optical lever sensitivity (invOLS) as the first.

The derivation has two principle steps. Firstly, dynamic force reconstruction is used to relate the cantilever's motion to the maximum force applied to the bilayer. Then, a contact mechanics model (in this case we use Hertz, $F \propto E_{\text{eff}}\delta^{3/2}$) can link the applied normal force, F , to the effective Young's modulus and indentation, δ . Many operating parameters are required to reconstruct the effective modulus, but only two vary across a bimodal scan: the first mode's instantaneous amplitude, A_1 , and second mode frequency shift, $\Delta\nu_2$. The others are determined before a scan is taken. The equations (evaluated for each pixel of a scan) were²⁴:

$$\delta = \frac{1}{2} \frac{k_1 \nu_2}{Q_1 k_2 \Delta\nu_2} (A_{0,1}^2 - A_1^2)^{1/2}, \quad (10)$$

$$E_{\text{eff}} = \frac{k_1}{Q_1 \delta^2} \sqrt{\frac{2A_1 (A_{0,1}^2 - A_1^2)}{R}}. \quad (11)$$

Here, k_1 and Q_1 are the stiffness and quality factor of the first mode, which are determined from the cantilever's thermal spectrum (see Fig. S7). k_2 and ν_2 are the stiffness and resonance frequency of the second mode and R is the radius of curvature of the tip, here taken to be 5 nm. $\Delta\nu_2$ is the shift in second mode frequency when moving the tip from the attractive to the repulsive regime close to the sample; $A_{0,1}$ (the first mode free amplitude) was evaluated at the same z -piezo height.

The imaging conditions were kept as similar as possible to those for which Fig. 1 & 3 were in the main text; small free (first mode) amplitudes of $A_{0,1} < 2 \text{ nm}$ and high setpoint ratios of $A_1/A_{0,1} > 70\%$. This ensured that, to the best of our ability, all topographic images presented in this manuscript are comparable. In fact, by imaging the same area of bilayer at progressively lower setpoints we were able to show that the extracted E_{eff}

is remarkably stable, and only begins to increase for very harsh imaging conditions of $A_1/A_{0,1} < 50\%$ (see Fig. S 8). This dramatic rise is to be expected, given that lower values of $A_1/A_{0,1}$ reflect larger forces being applied to the membrane, under which the stiff mica substrate will have progressively more impact on E_{eff} .

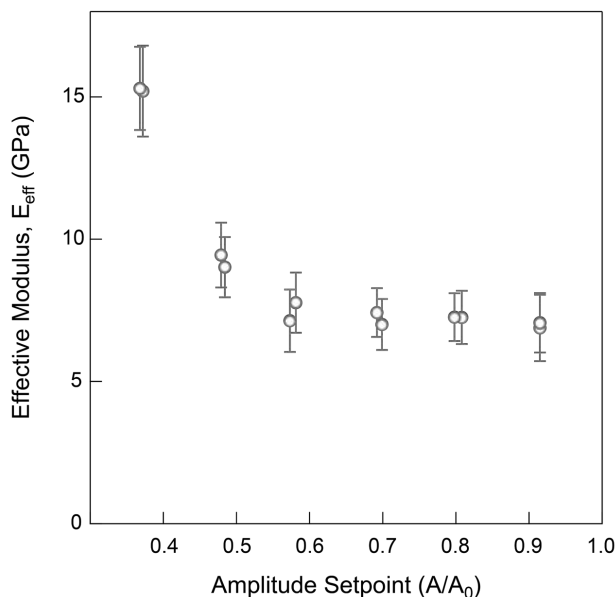


Fig. S 8 | Investigating the dependence of E_{eff} extracted from bimodal AFM on amplitude setpoint. The effective modulus is remarkably stable for $A_1/A_{0,1} > 0.5$, below which point, the increased force on the lipid bilayer results in the mica substrate having increasing influence on the stiffness.

3.5 Static force spectroscopy

To compare global membrane stiffness values of the lipids taken bimodally at high frequencies ($\nu_2 \sim 0.9$ MHz) with more conventional AFM methods, we performed force spectroscopy on a bilayer prepared identically to those above, with the same model of cantilever (in this case $k_1 = 6.58 \text{ Nm}^{-1}$). This was done without exciting the cantilever, in order to remove spurious effects that may occur due to driven motion of the tip. For each ionic solution, a map of 12×12 force curves were collected over an area of $100 \times 100 \text{ nm}^2$, in which the cantilever's deflection was recorded as a function of its z height above the sample. From this, force versus sample indentation curves were produced (as in Fig. S 9) using Asylum Research's analysis software (v14.30.157) for Igor, and knowledge of the cantilever's flexural stiffness and invOLS. From this, the same Hertz model as in section 3.4 could be applied and a comparable value for E_{eff} was extracted. The Asylum Research software was used to apply the model with the assumption that the tip had a spherical geometry with $R = 5 \text{ nm}$ and the bilayer's Poisson's ratio was $\nu_{\text{lipid}} = 0.33$. Then, the modulus was obtained from fits of force, F_{Hertz} , to indentation, δ , with equation 12.

$$F_{\text{Hertz}} = \frac{4\sqrt{R}}{3} \frac{E_{\text{eff}}}{1 - \nu_{\text{lipid}}^2} \delta^{3/2}. \quad (12)$$

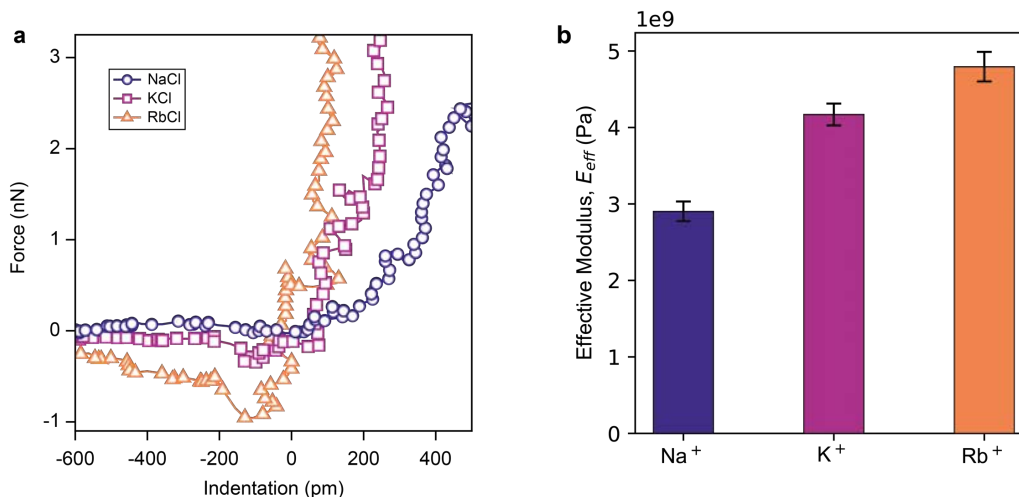


Fig. S 9 | Static force spectroscopy to validate bimodal results. (a): Exemplary AFM curves showing normal force versus indentation for a DPPA bilayer immersed in the three 150 mM ionic solutions. The variation in bilayer stiffness is highlighted in each ionic solution by the different rate of increase of the force with indentation. To quantify these differences, every curve in a 12×12 map was fitted with the Hertz model (equation 12) to extract the effective Young's modulus. The average of these values is displayed in (b) and agrees with the bimodal averages in the main script, both in order of magnitude and trend with ionic radius.

The results presented in Fig. 4 in the main text suggest that the DPPA membrane's Young's modulus is strongly dependent on the ionic content of the solution. The value of E_{eff} is inversely related to the binding constants of the ions present in Fig. 1e – that is, the higher the density of outer-sphere ions near to the bilayer, the softer it becomes. Thus, we expect that a similar effect can be obtained simply by reducing the ionic strength of the solution; i.e. as the concentration of Na^+ is reduced, the relative concentration of outer-sphere bound ions decreases, which we would expect to increase the global membrane stiffness. To confirm this, after collecting the data for Fig. S 9, we thoroughly rinsed the DPPA bilayer with different concentrations of NaCl buffer and performed identical static force spectroscopy experiments to find how this affected the measured stiffness. The results are presented in Fig. S10: the expected increase in stiffness with decreasing ionic strength is observed. This is in line with the conclusions presented in the main text, whereby the presence of outer-sphere ions displaces inner-sphere charges (in this case, H_3O^+), thereby softening the membrane.

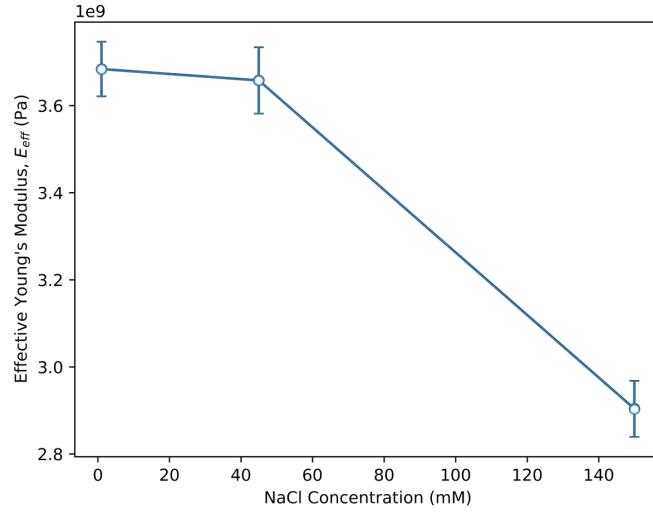


Fig. S 10 | Static force spectroscopy of the supported DPPA membrane in NaCl solutions of varying concentration. E_{eff} was calculated as earlier, from equation 12. The inverse relationship between ionic density in solution and the bilayer's stiffness support our conclusions presented in the main text, relating ionic domains to variations in Young's modulus.

4 Image analysis

The AFM topography phase and stiffness images presented in Fig. 1, 3 and 4 were all taken at original scan sizes of $(15 \times 5) \text{ nm}^2$, line-by-line flattened and then low-pass filtered for display to remove unwanted high-frequency noise. However, all quantitative analysis described below was carried out on the unfiltered images.

4.1 Roughness

The root mean-squared roughness, R_q of an image is defined as

$$R_q = \sqrt{\frac{1}{MN} \sum_{k=0}^{M-1} \sum_{l=0}^{N-1} z(x_k, y_l)^2}. \quad (13)$$

Here, the sums are over every row, k , and column, l , of the image and $z(x_k, y_l)$ is the height at the point (x_k, y_l) . In our case, the images had $M = N = 256$. The quoted roughness values are averages over 12 images for NaCl, 15 for KCl and 10 for RbCl.

4.2 Nearest neighbours distribution

Fig. S 11 illustrates the automated process used to arrive at a quantitative measure of how organised the adsorbed ion meshes were – that is, their nearest-neighbour (NN) distribution. First, the power spectrum of every $(15 \times 15) \text{ nm}^2$ image was used to generate an idealised reference lattice from which to define each lipid site in the bilayer. The image was then passed through a square averaging filter of 225 pixels (which approximately corresponded to the area per lipid at this level of zoom) in order to reduce the impact of image noise on the calculation. A histogram was then made of the pixels lying on the “ideal” lattice sites and fitted with a Gaussian function in order to determine the distribution's width, σ_s , and mean μ_s . The lattice sites were split into three categories depending on their height. “High” sites were defined as those with $z(x_k, y_l) > \sigma_s + \mu_s/2$ and interpreted as those sites where an alkali cation had successfully adsorbed in an outer-sphere complex (see main text). “Middling” sites had $\sigma_s - \mu_s/2 < z(x_k, y_l) < \sigma_s + \mu_s/2$ and “low” sites had $z(x_k, y_l) < \sigma_s - \mu_s/2$. The assignment of the latter two levels is less straightforward than the “high” sites, and so our analysis focussed only on those in the upper category. This automated routine was checked on each run to ensure that the categorisations reflected the real height distribution. Then, a simple procedure took each “high” site and counted how many adsorbed ions there were in a certain radius around it. By inspection (see e.g. Fig. S 11(e)), we found a radius of 0.65 nm gave the most accurate determination of the number of nearest neighbours for each site. The NN distribution was averaged over 12 images for NaCl imaging buffer and 15 for KCl. For RbCl, as only singly-adsorbed ions were observed, the NN distribution would have been trivial and so the calculation was not performed here.

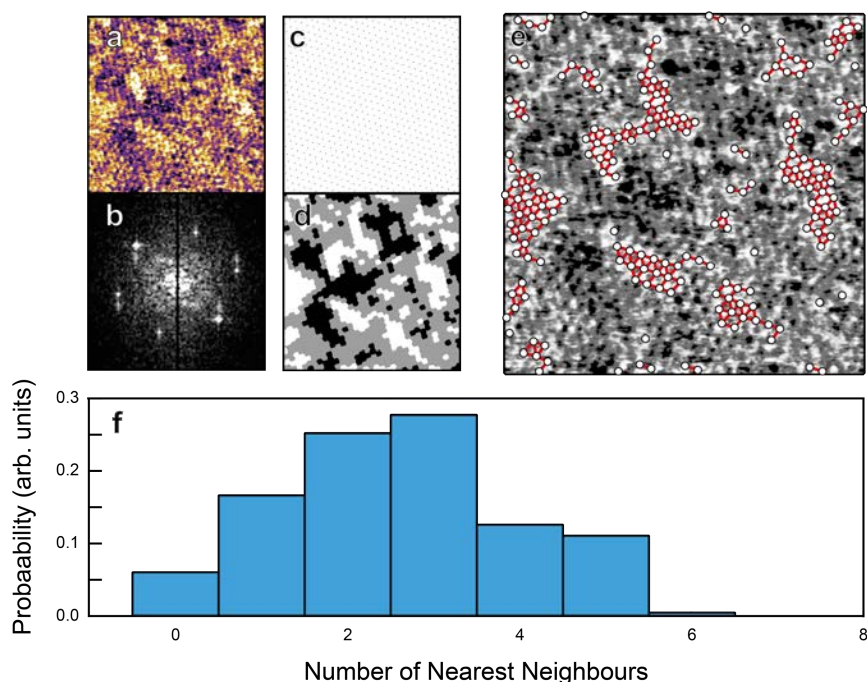


Fig. S 11 | Illustration of the procedure used to calculate the number of nearest neighbours for adsorbed ions on the lipid bilayer. (a) Original topography image used for analysis. (b) Zoomed power spectrum of corresponding phase image to that of (a). (c) Idealised lattice reconstructed from the power spectrum. (d) Voronoi mesh reflecting the three height levels observed in the original image. The height levels' thresholds were determined from the averaging procedure and Gaussian distribution of points as discussed in the text. (e) Each “high” lattice point (circles) was then checked for neighbours within a certain radius (here 6.5 Å); these are displayed as red lines between points. It can be seen that this choice of radius accurately captures the number of nearest neighbours (f) Resulting normalised NN distribution as calculated from (e). The averaged NN distributions for both K^+ and Na^+ ions are shown in Supplementary Fig. 12

To test whether the correlation between adsorbed ions was statistically greater than a theoretical random distribution of ions, an idealised lattice was generated for each image, in an identical manner to above. Once the initial categorisation of sites by their height was complete, a random number generator was used to mix the site categories, thus shuffling the distribution. The newly-mixed “high” sites were duly put through the same NN analysis, with the same parameters used in all cases. The results from both these analyses for K^+ and Na^+ ions are shown in Fig. S 12. The mean number of nearest neighbours, μ_{K^+} , μ_{Na^+} , in each situation was then found from Gaussian fits to the histograms (solid lines in Fig. S 12) and the errors were those taken as the fitting uncertainties generated by Igor v6.3.7.2.

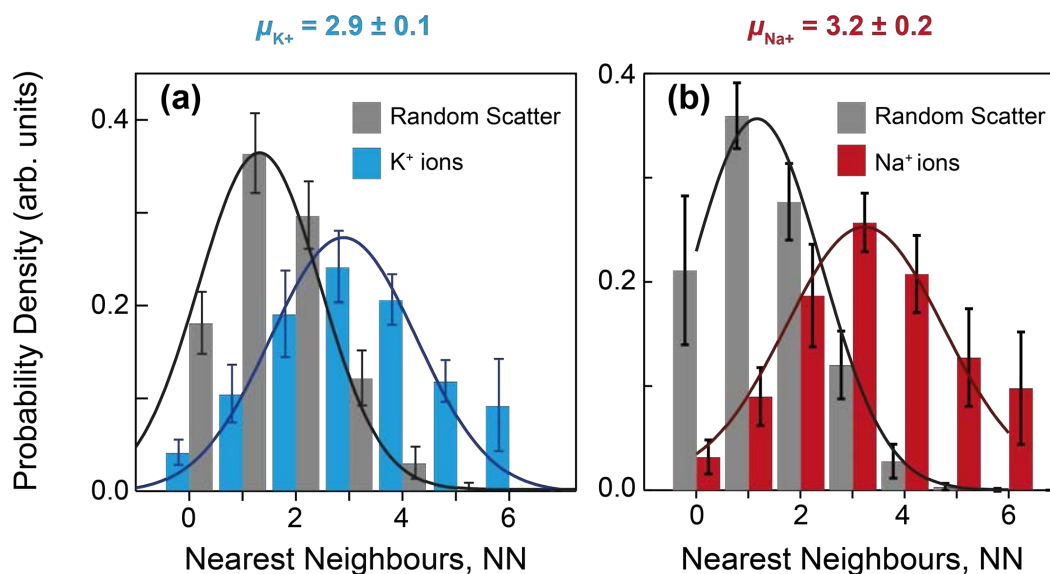


Fig. S 12 | Comparing nearest neighbour distributions for adsorbed potassium (a) and sodium (b) ions with a random distribution of equivalent coverage. In both cases, the ions form organised domains on the bilayer that have higher μ than random distributions. Fitting the histograms with Gaussian functions gives $\mu_{K^+} = 2.9 \pm 0.1$ and $\mu_{Na^+} = 3.2 \pm 0.2$.

4.3 Ionic decorrelation time, τ

To evaluate the change of the domains over time, it was necessary to find the ions' correlation function, $\Lambda(\Delta t)$, and how this depended on the number of nearest neighbours. Thus, the automated procedure of section 4.2 was performed on consecutive AFM images, which gave a list of the locations and NN of adsorbed ions at different timesteps. In order to increase the temporal resolution beyond the $\Delta T \sim 32$ s between individual AFM frames, we used the time per scan line and scan direction to determine the precise time between the tip returning to each lattice site, Δt . Once this time gap had been computed, we checked whether the site still had an ion remaining there and, if so, how many nearest neighbours it had in the initial frame. This allowed us to build up a histogram of the time taken for ions to desorb/diffuse and quantitatively assess how this depended on the number of nearest neighbours for times up to ~ 120 s. After populating the histogram, the data was normalised using the total number of ions for a given number of nearest neighbours within each Δt bin – i.e. not just those that did not desorb or diffuse along the membrane. Thus, the correlation function for $\Delta t = 0$ in Fig. 3 is unity by definition. To extract Λ from the correlation functions, a function of the form $\Lambda(\Delta t) = y_0 + A \exp(-\Delta t/\tau)$, where y_0 and A are constants, was fitted to $\Lambda(\Delta t)$ and τ was plotted as a function of NN in Fig. 3's inset.

5 Molecular dynamics (MD) simulations

5.1 Methods, description of simulated systems and simulation protocol

We considered three different simulations, with the compositions given in

Table II. In all cases, we considered a bilayer of anionic DPPA-lipid in water containing 136 lipid molecules (68 DPPA molecules at each leaflet) and different ionic compositions. The ions included in simulations SimA, SimB and SimC (see Table I) were lipid counterions (Na^+ , K^+ or Rb^+ respectively) and added salt (NaCl , KCl and RbCl respectively).

| | Cations | Anions | Waters | DPPA ⁻ | Total Atoms | Bilayer Surface Area (nm ²) |
|------|-------------------|------------------|--------|-------------------|-------------|---|
| SimA | 156 Na^+ | 20 Cl^- | 6463 | 136 | 30231 | 30.0 |
| SimB | 156 K^+ | 20 Cl^- | 6463 | 136 | 30231 | 30.3 |
| SimC | 150 Rb^+ | 20 Cl^- | 6463 | 136 | 30213 | 30.5 |

Table II |Composition of the systems considered in the MD simulations, including number of molecules and total number of atoms and equilibrium area of the bilayer.

In our simulations, we describe all chemical species (water, lipids and ions) and their interactions with full atomistic detail using the CHARMM36 force field. For water, we employed the TIP3P parameters, standard in CHARMM36. In all simulations, we considered that each DPPA molecule has a net charge of -1 , with atomic partial charges given by standard values of the CHARMM36 force field. In the case of ions, we used the improved CHARMM36 parameters proposed in Ref²⁶.

We build the simulated systems as follows. First, we generated a DPPA bilayer of area $65.45 \text{ \AA} \times 65.45 \text{ \AA}$ with 136 lipid molecules using the CHARMM-GUI membrane builder²⁷. Using VMD²⁸, we added solvation water and ions, with the amounts indicated in

Table II. We used the ionize plugin of the VMD program to automatically add the number of ions corresponding to 150 mM of salt. The configurations obtained in this way were energy minimized using NAMD 2.11 software²⁹.

Once the initial configurations were prepared, we performed MD simulations using NAMD 2.11 software. The Newtonian equations of motion were solved using a time step of 2 fs. Electrostatic interactions were computed using the particle mesh Ewald method (PME) with usual settings in NAMD (1 \AA resolution, updated each 2 time steps). Lennard-Jones interactions were truncated at 1.2 nm, employing a switching function starting at 1.0 nm. Periodic boundary conditions were employed in all directions. Temperature was kept constant at 298 K using a Langevin thermostat with a relaxation time of 1 ps. A pressure of 1 atm in the

direction perpendicular to the bilayer was imposed using the anisotropic Nosé-Hoover-Langevin piston implemented in NAMD (oscillation period of 100 fs and decay time of 50 fs). The lateral pressure imposed by the barostat was adjusted to maintain the bilayer at zero tension, so our simulations correspond to the NPT γ ensemble. For each case shown in

Table II, we performed ~ 20 ns of equilibration simulation and ~ 100 ns of production simulation.

5.2 Analysis of MD results: technical details and additional results

The first magnitude analyzed in the production simulations was the area per molecule, averaged over all the production run (Table I). As seen in Table I, the results for all ions were very similar, as should be expected in the ordered gel phase.

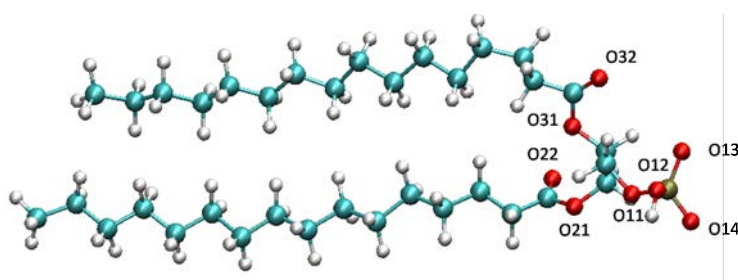


Fig. S 13 | Scheme of the DPPA lipid in CPK representation with labels indicating the atom names given to the oxygen atoms (in red) in the molecule.

The adsorption of the ions at the DPPA-water interface was analysed by computing the radial correlation functions, $g(r)$, between the cations and the lipid oxygen atoms (see Fig. S 13 for atom naming definitions and Figures S14 to S17 for the $g(r)$ functions).

As shown in these figures, there are clear correlations (corresponding to ion adsorption) between cations and oxygen atoms. The details of these correlations depend on the particular cation and also on the particular oxygen atoms (not all of them are equivalent, as seen in Figures S13 to S17). In all cases, we can clearly see two or even three correlation peaks. The first peak in these functions corresponds to the direct adsorption of the cations to lipids with an oxygen atom from lipids in the first coordination shell of the cations. The second peak in these functions is due to two different contributions. In some cases, the secondary peak simply takes into account cations which have another lipid oxygen in the first coordination shell (so the peak simply reflects the molecule geometry). However, in most of the cases (particularly for $g(r)$ functions corresponding to the external headgroup lipid oxygen atoms O13 and O14), the secondary peak correspond to a cation that does not have any lipid oxygen atom in the first coordination shell. In this case, the cation shares a water molecule with DPPA (i.e. it has a water molecule in its first coordination shell that is also present in the first coordination shell of an oxygen from the DPPA lipid). These adsorbed cations are the ones designated as “outer sphere” adsorbed ions in the main paper.

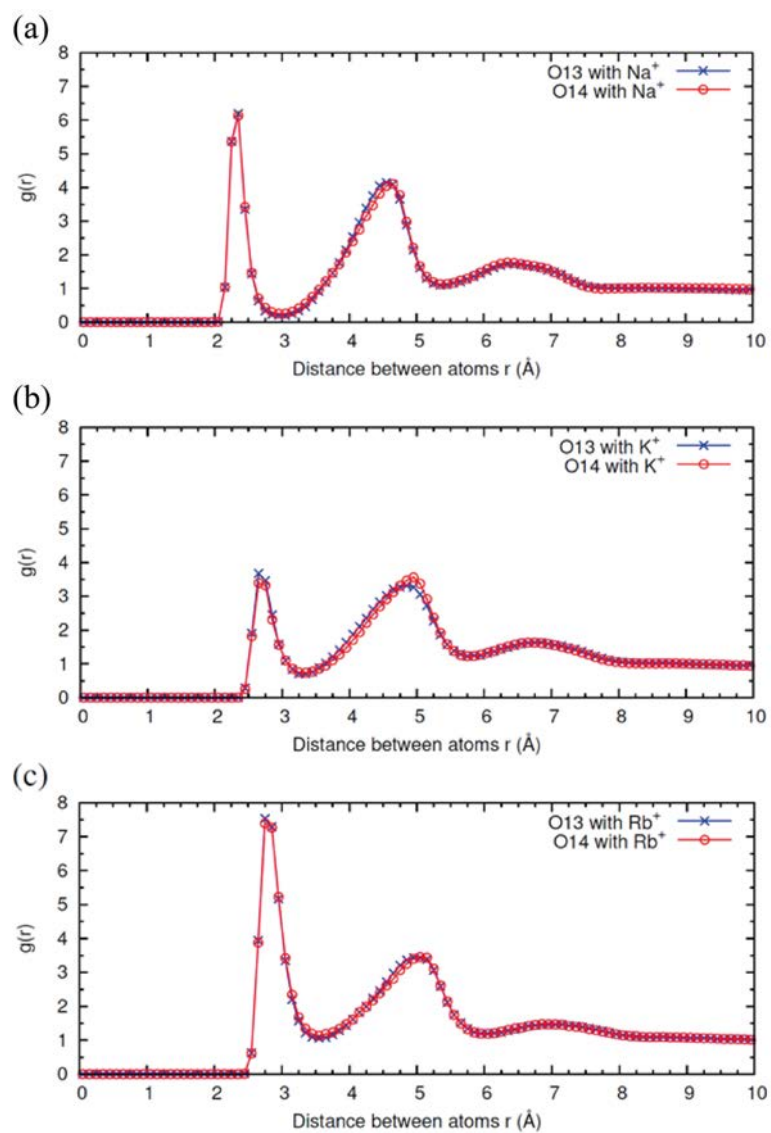


Fig. S 14 | Radial correlation functions, $g(r)$, computed in MD simulations between the cations and the DPPA headgroup external oxygen atoms O13 and O14 (see Fig. S13).

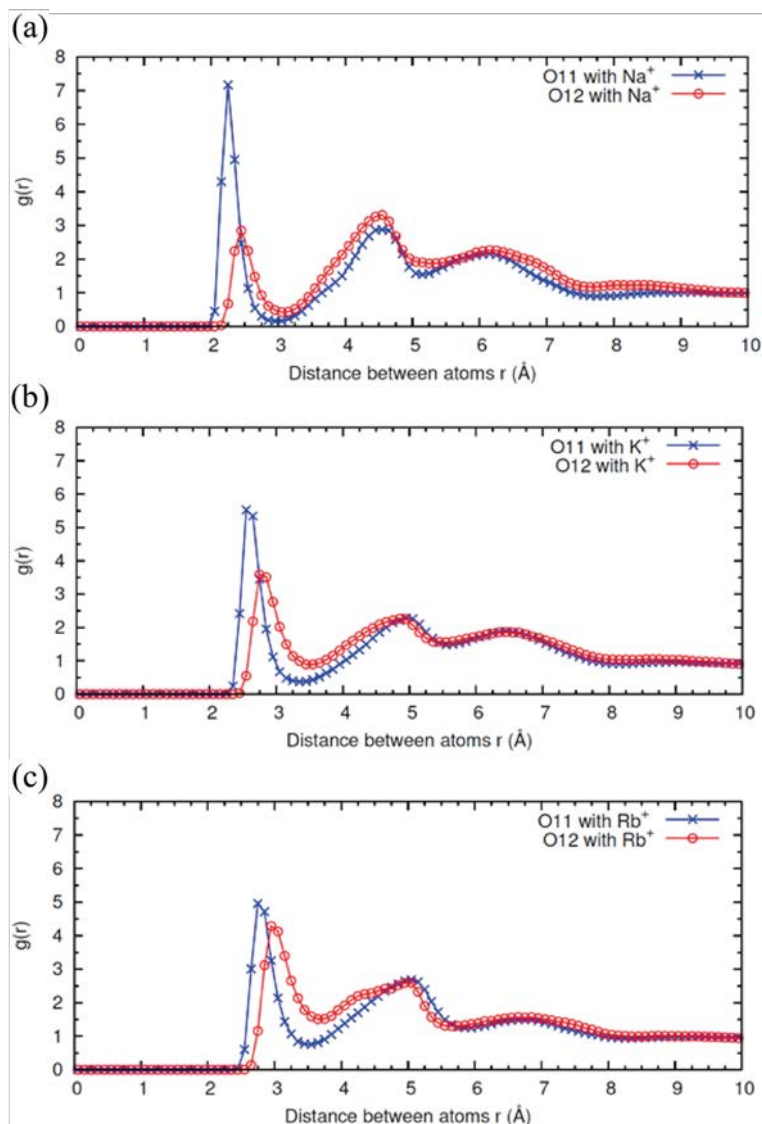


Fig. S 15 | Radial correlation functions, $g(r)$, computed in MD simulations between the cations and the DPPA headgroup oxygen atoms O11 and O12 (see Fig. S13).

In order to identify the different contributions, we used a homemade analysis program that examined the environment of each cation and allows us to identify and quantify these different binding modes. These are the results reported in Fig. 2 in the main paper. Particular configurations showing these different kinds of adsorbed cations for sodium, potassium and rubidium are also shown in Fig. S 18. Note in these figures the absence of Cl^- anions. In our simulations, we do not find anions in the first coordination shell of adsorbed cations or in the first coordination shell of lipids, indicating that anions do not play a role in the observed structures. Test simulations without added salt that contain only cations as counterions of DPPA^- (not shown) show identical adsorption modes of potassium, sodium and rubidium cations as described here.

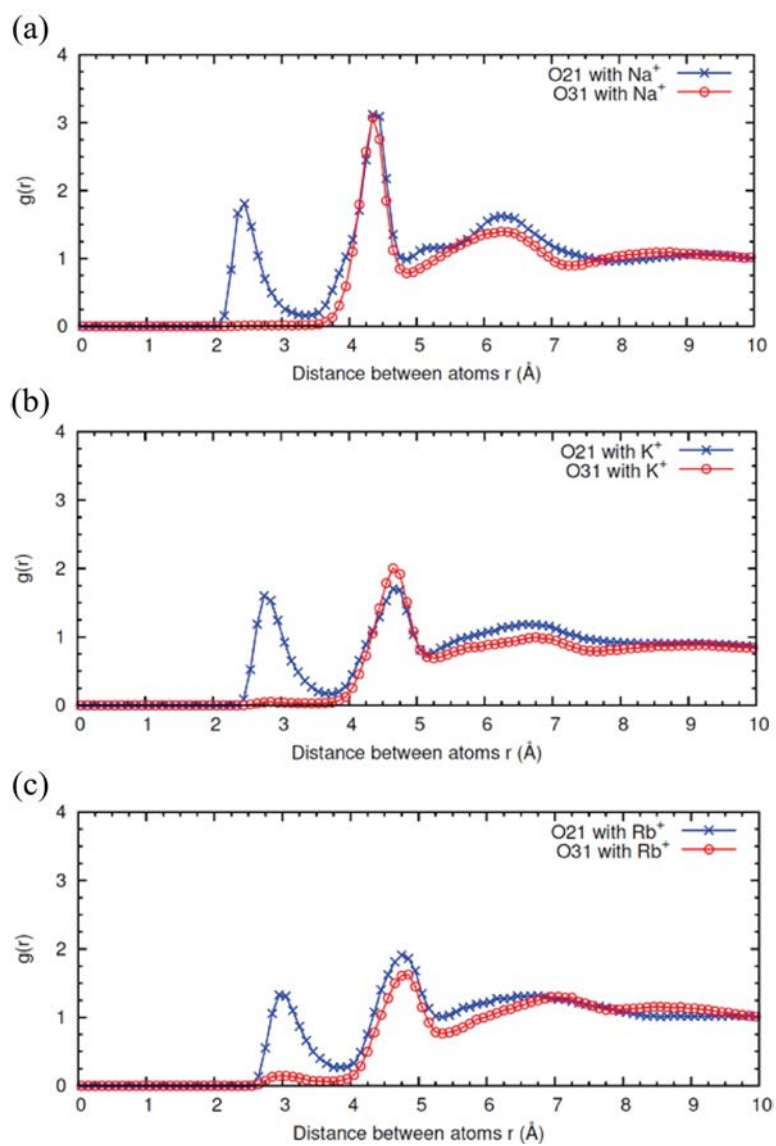


Fig. S 16 | Radial correlation functions, $g(r)$, computed in MD simulations between the cations and the DPPA oxygen atoms O21 and O31 (see Fig. S13).

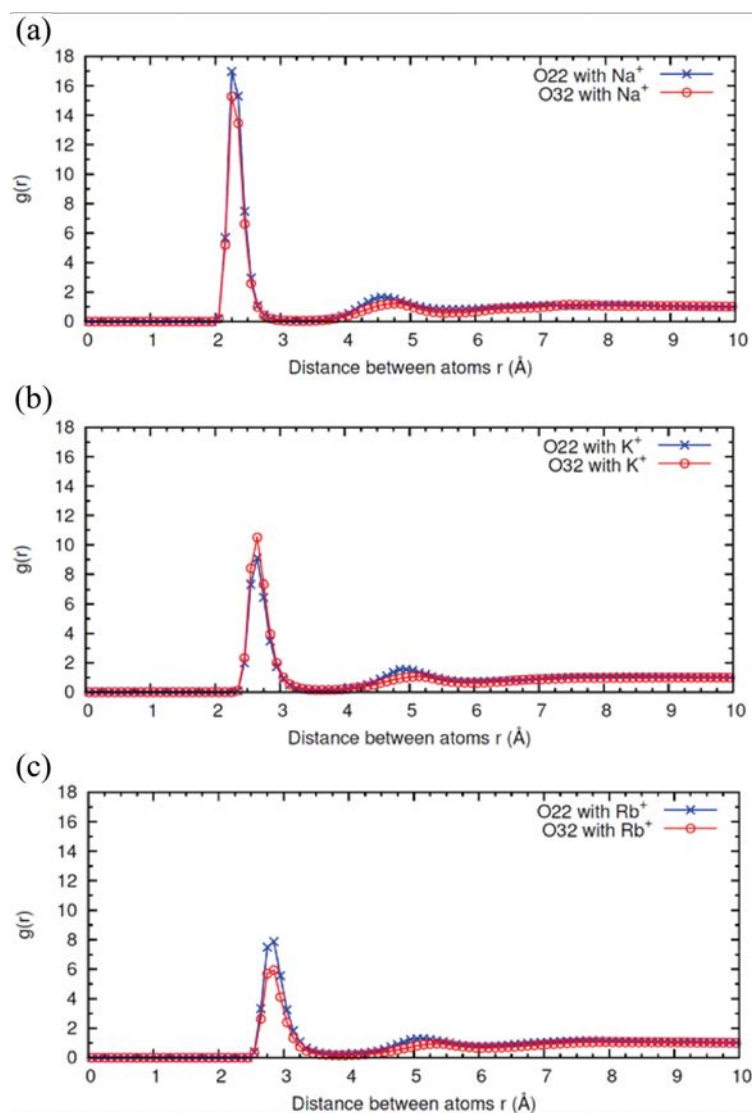


Fig. S 17 | Radial correlation functions, $g(r)$, computed in MD simulations between the cations and the DPPA oxygen atoms O22 and O32 (see Fig. S13).

We have also calculated the radial correlation functions between cations and water oxygen atoms and between oxygen lipids and water hydrogen atoms (not shown) in order to study the hydration of cations and lipids. The analysis of the composition of the coordination shell and the hydration of cations reveal also further differences between them, as shown in

Table **III**. It is interesting to note that the first coordination shell of Na^+ is the only one that remains unaltered after adsorption. It contains an average of 5.3 oxygen atoms from water for both free Na^+ ions in bulk water and Na^+ ions adsorbed in the outer shell (ions indicated in yellow in Fig. 2 and S18) and also 5.3 oxygen atoms (from lipid oxygens and water oxygens) in the case of Na^+ ions adsorbed in the inner shell (green ions in Fig. 2

and Fig. S 18). For both K^+ and Rb^+ , the solvation shell contracts from being at bulk to adsorption for ions adsorbed in the outer shell and expands in the case of ions adsorbed in the inner coordination shell.

| | Bulk ions | Adsorbed ions (outer sphere) | Adsorbed ions (inner sphere) |
|---------------|-----------|------------------------------|------------------------------|
| Na^+ (SimA) | 5.3 | 5.3 | 5.2 (2.0 + 3.3) |
| K^+ (SimB) | 6.1 | 6.5 | 6.5 (2.5 + 4.0) |
| Rb^+ (SimC) | 6.8 | 7.2 | 7.2 (2.8 + 4.4) |

Table III | Average number of oxygen atoms in the first coordination shell of cations as computed in MD simulations. In the case of ions in bulk solution and ions adsorbed in the outer shell of the DPPA bilayer, these oxygen atoms belong to water molecules. In the case of ions adsorbed in the inner shell of DPPA bilayer, the oxygen atoms belong to lipids (first number in parenthesis) or to water molecules (second number in parenthesis).

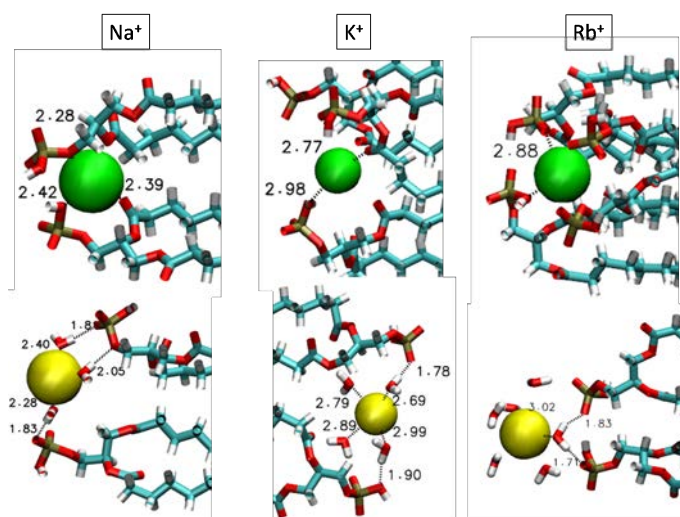


Fig. S 18 | Snapshots of MD simulations showing the details of cation adsorption onto a DPPA bilayer in the presence of added salt (NaCl, KCl or RbCl respectively). The colour of the ions indicates the adsorption mode: green corresponds to cations coordinated to lipid oxygens and yellow corresponds to cations that share hydration water molecules with lipids. As in the main paper, DPPA lipids are shown in bonds representation and ions are shown as Van der Waals spheres. The employed colour code for DPPA corresponds to the standard crystallographic CPK convention (red: oxygen, white: hydrogen, cyan: carbon, phosphorous: orange). Some cation hydration water molecules are also shown in the bottom images (all water molecules shown are shared by cation and DPPA in the case of Na^+ and K^+). Some ion-lipid oxygen, ion-oxygen water and hydrogen water-lipid oxygen distances are also indicated (in Å).

6 Supplementary References

- 1 W. Trewby, D. Livesey and K. Voitchovsky, *Soft Matter*, 2016, **12**, 2642–2651.
- 2 M. M. A. E. Claessens, B. F. Van Oort, F. A. M. Leermakers, F. A. Hoekstra and M. A. C. Stuart, *Biophys. J.*, 2004, **87**, 3882–3893.
- 3 D. Marsh, *CRC Handbook of Lipid Bilayers*, CRC Press, Second., 2013.

- 4 M.-P. Mingeot-Leclercq, M. Deleu, R. Brasseur and Y. F. Dufrêne, *Nat. Protoc.*, 2008, **3**, 1654–1659.
- 5 R. Richter, A. Mukhopadhyay and A. Brisson, *Biophys. J.*, 2003, **85**, 3035–47.
- 6 I. Reviakine and A. Brisson, *Langmuir*, 2000, **16**, 1806–1815.
- 7 A. Alessandrini and P. Facci, *Soft Matter*, 2014, **10**, 7145–7164.
- 8 J. C. Berg, *An Introduction to Interfaces and Colloids: The Bridge to Nanoscience*, World Scientific Publishing Co., 1st edn., 2009.
- 9 J. N. Israelachvili, *Intermolecular and Surface Forces*, Elsevier, Third., 2011.
- 10 P. Maity, B. Saha, G. S. Kumar and S. Karmakar, *Biochim. Biophys. Acta - Biomembr.*, 2016, **1858**, 706–714.
- 11 S. McLaughlin, N. Mulrine, T. Gresalfi, G. Vaio and A. McLaughlin, *J. Gen. Physiol.*, 1981, **77**, 445–73.
- 12 M. Eisenberg, T. Gresalfi, T. Riccio and S. McLaughlin, *Biochemistry*, 1979, **18**, 5213–5223.
- 13 M. Ricci, P. Spijker and K. Voitchovsky, *Nat. Commun.*, 2014, **5**, 4400.
- 14 G. Cevc, *Biochim. Biophys. Acta*, 1990, **1031**, 311–382.
- 15 H. J. Butt and M. Jaschke, *Nanotechnology*, 1995, **6**, 1.
- 16 Y. S. Lo, N. D. Huefner, W. S. Chan, P. Dryden, B. Hagenhoff and T. P. Beebe, *Langmuir*, 1999, **15**, 6522–6526.
- 17 E. J. Miller, W. Trewby, A. Farokh Payam, L. Piantanida, C. Cafolla and K. Voitchovsky, *J. Vis. Exp.*, 2016, 1–10.
- 18 R. García and R. Pérez, *Surf. Sci. Rep.*, 2002, **47**, 197–301.
- 19 K. Kobayashi, Y. Liang, K. I. Amano, S. Murata, T. Matsuoka, S. Takahashi, N. Nishi and T. Sakka, *Langmuir*, 2016, **32**, 3608–3616.
- 20 E. Rudolphi-Skórska, M. Zembala and M. Filek, *J. Membr. Biol.*, 2014, **247**, 81–92.
- 21 U. M. Ferber, G. Kaggwa and S. P. Jarvis, *Eur. Biophys. J.*, 2011, **40**, 329–338.
- 22 H. Asakawa and T. Fukuma, *Nanotechnology*, 2009, **20**, 264008.
- 23 M. Ricci, P. Spijker, F. Stellacci, J.-F. Molinari and K. Voitchovsky, *Langmuir*, 2013, **29**, 2207–2216.
- 24 C. A. Amo, A. P. Perrino, A. F. Payam and R. Garcia, *ACS Nano*, 2017, **11**, 8650–8659.
- 25 A. F. Payam, W. Trewby and K. Voitchovsky, *Appl. Phys. Lett.*, 2018, **112**, 083101.
- 26 J. Yoo and A. Aksimentiev, *Phys. Chem. Chem. Phys.*, 2018, **20**, 8432–8449.

- 27 E. L. Wu, X. Cheng, S. Jo, H. Rui, K. C. Song, E. M. Dávila-Contreras, Y. Qi, J. Lee, V. Monje-Galvan, R. M. Venable, J. B. Klauda and W. Im, *J. Comput. Chem.*, 2014, **35**, 1997–2004.
- 28 W. Humphrey, A. Dalke and K. Schulten, *J. Mol. Graph.*, 1996, **14**, 33–38.
- 29 J. C. Phillips, R. Braun, W. Wang, J. Gumbart, E. Tajkhorshid, E. Villa, C. Chipot, R. D. Skeel, L. Kalé and K. Schulten, *J. Comput. Chem.*, 2005, **26**, 1781–1802.